Microscale processes determining macroscale evolution of magnetic flux tubes along Earth's magnetopause

K.-J. Hwang[1], J. L. Burch[1], C. T. Russell[2], E. Choi[1], K. Dokgo[1], R. C. Fear[3], S. A. Fuselier[1], S. M. Petrinec[4], D. G. Sibeck[5], H. Hasegawa[6], H. Fu[7], M. Øieroset[8], C. P. Escoubet[9], B. L. Giles[5], R. J. Strangeway[2], Y. Khotyaintsev[10], D. B. Graham[10], D. J. Gershman[5], C. J. Pollock[11], R. E. Ergun[12], R. B. Torbert[13], and J. Broll[14]

[1] Southwest Research Institute, San Antonio, TX, USA
[2] Institute of Geophysics and Planetary Physics, University of California, Los Angeles, Los Angeles, CA, USA
[3] University of Southampton, Southampton, UK
[4] Lockheed Martin Advanced Technology Center, Palo Alto, CA 94304, USA
[5] NASA Goddard Space Flight Center, Greenbelt, MD, USA
[6] Institute of Space and Astronautical Science, Japan Aerospace Exploration Agency, Sagamihara, Japan
[7] School of Science and Environment, Beihang University, Beijing, China
[8] Space Sciences Laboratory, University of California, Berkeley, Berkeley, CA, USA
[9] European Space Agency, the Netherlands
[10] Swedish Institute of Space Physics, Uppsala, Sweden
[11] Denali Scientific, LLC, Fairbanks, AK, USA
[12] Laboratory for Atmospheric and Space Physics, University of Colorado at Boulder, Boulder, CO, USA
[13] Space Science Center, University of New Hampshire, Durham, NH, USA
[14] Center for Space Physics, Boston University, Boston, MA, USA

Corresponding author: Kyoung-Joo Hwang (jhwang@swri.edu)

Abstract

An important process affecting solar wind-Earth's magnetosphere coupling is non-steady dayside magnetic reconnection, observationally evidenced by a flux-transfer-event (FTE) that shows a bipolar variation of the magnetic field component normal to the magnetopause. FTEs often consist of two interlinked flux tubes, but, local kinetic processes between the flux tubes are not understood in the context of the FTE structuring, evolution, and impact. An FTE observed by MMS on 18 December 2017 consisted of two flux tubes of different topology. One includes field lines with ends connected to the northern and southern hemispheres while the other includes field lines with both ends connected to the magnetosheath. Reconnection occurring at the flux-tube interface indicates how interacting flux tubes evolve into a flux rope with helical magnetic topology that is either closed or open. This study demonstrates a new aspect of how micro-to-meso-scale dynamics occurring within FTEs determines their macroscale characteristics and evolution.

Introduction

Solar wind-magnetosphere coupling often occurs in a localized and transient manner, modifying the magnetosphere-ionosphere system. One of the most common and important processes underlying such transient phenomena is non-steady dayside magnetic reconnection. Contrary to continuous or quasi-steady reconnection, transient reconnection gives rise to a localized structure of enhanced magnetic flux. This structure forms and convects over the surface of Earth's magnetosphere called the magnetopause, due to the combination of the anti-sunward magnetosheath flow and tension force exerted on the reconnected flux tube[1]. The observational evidence of such transient structures is a bipolar signature in the magnetic field component normal to the magnetopause (B_N) associated with the drifting motion (see dashed blue arrows in Fig. 1a).

Since Russell and Elphic[2] termed this signature a flux transfer event (FTE), numerous *in-situ* observations have determined their typical signatures. In addition to the B_N reversal, these signatures include enhanced magnetic field strength (B) due to a strong core field, an increase in the total pressure, and a mixture of magnetosphere and magnetosheath plasmas. These signatures have been explained by their generation via 1) localized bursts of dayside reconnection[2], 2) multiple X-lines[3], or 3) temporal modulation of the reconnection rate during continuous single X-line reconnection[4]. The different generation mechanisms give rise to different magnetic field topology and connectivity to either the northern or southern hemisphere or the magnetosheath (the shocked and slowed solar wind across Earth's bow shock). On the other hand, they commonly invoke formation processes occurring over macroscopic scales, resulting in FTEs with macroscale sizes comparable to one Earth radius (R_E)[5].

Recent observations using the data from the Magnetospheric Multiscale mission (MMS)[6] with its high-resolution measurements and tetrahedral configurations with spacecraft separations varying from a couple of d_i (ion inertial lengths) to a few d_e (electron inertial lengths) have enabled detailed investigations of kinetic boundaries and physical processes occurring within/around FTEs. The observations include evidence for 1) ion-scale secondary flux ropes generated by dayside reconnection[7,8], 2) multi-layered substructures within an FTE[9], 3) electron- or ion-scale current layers at the interface of two coalescing FTEs[10,11], 4) reconnection between colliding reconnection jets in a compressed current sheet at the center of an FTE[12], 5) reconnecting current sheet between interlinked flux tubes[13,14], and 6) the formation of an FTE driven by the electron vortex[15]. These observations indicate that microscale (electron) and mesoscale (ion) physical processes occurring in/around FTEs play a crucial role in the generation, structure, and evolution of FTEs.

These local kinetic processes, however, have not received sufficient attention in FTE formation, structuring, and evolution. Yet, they can be essential ingredients in the dynamics of FTEs that may grow into large-scale FTEs drifting down the tail along the magnetopause, forming the basis of magnetospheric activities such as geomagnetic storms and substorms. Thus, the localized physics occurring in FTEs may be key to understanding solar wind-magnetosphere coupling and the global magnetospheric system, which has not yet been explored.

This paper presents a new aspect of kinetic processes occurring within FTEs. These kinetic processes can lead to the topological structure and evolution of FTEs (Fig. 1d-e), implying the effect of micro-to-meso-scale dynamics occurring within FTEs on the macroscale characteristics of FTEs. We use an FTE event observed by the MMS on the dayside magnetopause on 18 December 2017 to illustrate this new aspect of FTEs. The detailed plasma and field data indicate that the FTE consists of two interlaced flux tubes. Using particle distributions and force analysis, we investigate topological signatures of the FTE and discuss the kinetic processes occurring at the interface of the two flux tubes that lead to the formation of a large-scale flux rope connecting both hemispheres, therefore, potentially regulating magnetic flux transfer into the magnetotail.

Results

Propagation, observation location, and scale size of the event. The MMS spacecraft was located at [9.0, -1.2, 1.3]R_E in Geocentric Solar Magnetospheric coordinates (GSM) at ~08:15:00 UT on 18 December 2017. Figs. 2 and 3 present field and particle observations by MMS over 8 s from 08:14:59 UT to 08:15:07 UT. During this period the interplanetary magnetic field (IMF) obtained from ARTEMIS-C was relatively steady, pointing mostly due duskward and southward: [1.8, 8.0, -4.0] nT (not shown) in GSM. The tetrahedral-averaged magnetic field using the measurements from the four MMS spacecraft (Fig. 2a; B_X, B_Y, and B_Z components shown as blue, green, and red profiles), together with the magnetic strength (B; black) shows that B_X exhibits a bipolar signature, around which B increases, indicating an FTE.

All vector parameters displayed in Fig. 2(d-k) and 3 are shown in boundary normal coordinates (LMN; see the top of the right panel of Fig. 1a) that were determined from minimum variance analysis (MVA)[16] and MDD[17]: L = [0.39, -0.61, 0.69], M = [0.45, -0.52, -0.72], N = [0.80, 0.60, 0.07] in GSM. M, indicating the axis of an FTE, has a large fraction along Z. This indicates a significant deviation of LMN for the present event from nominal magnetopause LMN coordinates (see black arrows in Fig. 4a). The panels of Fig. 2 are obtained using the measurements from the four MMS spacecraft with an average separation of 31.6 km. Fig. 3A and B show MMS4 and MMS2 observations, respectively.

At ~08:15:03.2 UT, B_N (red profile in Fig. 2d and Fig. 3a) changed from negative to positive (vertical dashed black line, 'C' shown on the top of Fig. 2 and 3). Coincidentally, the magnetic field strength (B, black profile) increased. These magnetic perturbations are associated with the overall motion of an FTE along -L (see the dashed blue arrow in Fig. 1a that represents a relative trajectory of the spacecraft across an FTE mostly along L, observing a negative, and then, positive B_N). To investigate the propagation of the FTE, we performed multiple triangulation analysis (MTA)[18] using a four-spacecraft timing analysis[19,20]. The direction of the propagation vector was duskward and southward: [-0.45, 0.54, -0.71] in GSM or [-0.99, 0.07, -0.14] in LMN, with a speed of 204 km/s. This result is consistent with the prediction from the maximum shear model[21] using the solar wind IMF condition for this event. White traces in Fig. 4(a) show primary X-lines over the surface of the magnetopause when viewed from the Sun. A component reconnection X-line is located dawnward and northward of the MMS location (blue rectangle), leading to a duskward and southward motion of an FTE (black lines departing from the blue rectangle). The MTA-derived propagation vector (thick magenta arrow in Fig. 4a) together with the L and M axes (black arrows) shows a good agreement between the observation and the model prediction. Fig. 4(b) illustrates the FTE structure (to be detailed below) embedded in the southern outflow region of the X-line when viewed mostly from the -M direction.

We define the location where B_N becomes negative before the B_N reversal as the leading boundary of the FTE ('L' at the top of Fig. 2 and 3, marked by vertical dashed magenta line) and the location where B_N is reduced after the B_N reversal as the trailing boundary of the FTE ('T' at the top of Fig. 2 and 3, marked by vertical dashed cyan lines). The cross-sectional scale of the FTE is then estimated to be 736 km, which is ~12.2 d_i (ion inertial length: ~60 km for this event). The existence of the X-line above the FTE along L is also evidenced by the ion PAD (Fig. 3f).

When B_L fluctuated around zero between ~'L' and 'T' (Fig. 3a), the ion flow mostly directed perpendicularly to **B**. When B_L was negative before ~'L' (positive around/after 'T'), the ion PAD exhibited a significant parallel flux (mostly perpendicular and slightly anti-parallel flux). This is consistent with thin magenta arrows along with the MMS trajectory (dashed cyan arrow) in the Fig. 4(b) illustration.

Observation of the FTE consisting of two interlinked flux tubes. While the B_N and B profiles suggest a typical southward-moving FTE across the spacecraft, we note a consecutive weak variation of a negative-to-positive B_L during 'L'-'C' and 'C'-'T', as marked by '1', '2', '3', and '4' in Fig. 2(d) and 3(a). The most invariant axis (Fig. 2b) is primarily along X for the earlier interval ('L'-'C'), but significantly toward Y and Z for the later interval ('C'-'T'). When averaged over each interval under the error indicator (Fig. 2c) ≤ 0.5, the invariant axis in LMN directs to [-0.24, -0.38, -0.89] for 'L'-'C', and [0.01, -0.83, 0.56] for 'C'-'T'. This result is consistent with the result from MVA, particularly for 'C'-'T', during which the bipolar B_L signature is clearer (Fig. 2d). The two invariant axes make an angle of 79.3°. This observation indicates that the FTE consisted of the two flux tubes[22]. Fig. 4(b) shows a schematic diagram of the two flux tubes oriented almost perpendicularly. Numbers, '1', '2', '3', and '4' as observed by MMS crossing the structure along the trajectory (dashed cyan arrow) correspond well to those in Fig. 2(d) and 3(a).

Plasma parameters also show notable differences across 'C': ion density (temperature) is lower (higher) during the interval between 'L' and 'C' than between 'C' and 'T' (Fig. 3b); $V_{i,M}$ changes from negative to positive across 'C' (green arrows in Fig. 3c). Most importantly, we note that the electron PAD exhibit dramatic changes across 'C': the low and mid energy electron fluxes (Fig. 3j, k) were lower between 'L' and 'C' than between 'C' and 'T'; 90° pitch-angle electrons often greatly enhanced in the high-energy range (Fig. 3l) only before 'C'. These significant differences in the electron PAD across the FTE center indicate two interlaced flux tubes[14]: the intense 90°-focused energetic population is likely to be trapped on the field lines connected to both hemispheres (supported by the low density and high temperature of the plasma in Fig. 3b; to be discussed below); the absence or reduction of such populations between 'C' and 'T' indicates magnetosheath field lines or open field lines that allow hot magnetospheric populations to escape. Completely different magnetic connectivity before and after the center of the FTE inferred from the electron PAD strongly supports the interpretation of two interlinked flux tubes, instead of a single flux-rope-type FTE (such as an FTE illustrated in Fig. 1a).

For a commonly observed relatively force-free flux rope[38] ($\mathbf{J}\times\mathbf{B}\approx 0$), the current density is mostly parallel to **B** ($J_{||} > J_{\perp}$). Both the curl of the magnetic field and the curl of mostly field-aligned flow vectors are predicted to be symmetric for the axial (M) component (with a single peak at the center) and bipolar for the tangential (L or N) component across the center. During ~08:15:3.1-3.6 UT around 'C', $J_{||}$ is significantly greater than $J_{\perp}$ (Fig. 2f). The predicted signature is, however, ambiguous in the current density (Fig. 2e) and even opposite in the ion vorticity (bipolar $\Omega_{i,M}$ and relatively symmetric $\Omega_{i,N}$ in Fig. 2k) across ~'C'. $J_{||}$ shows double peaks around 'C', instead of a single peak (blue arrows in Fig. 2f). These peaks coincide with bipolar peaks in $\Omega_{i,M}$ (green arrows in Fig. 2k). Also, the magnetic curvature (Fig. 2h-j) that is expected to be bipolar along L and N across the center of a typical flux rope, exhibits complicated profiles, in particular, showing consecutive bipolar signatures in the L component (Fig. 2h). These observations further support that the present FTE consisted of two flux tubes.

Reconnection at the interface of two interlinked flux tubes. At the center of the B_N reversal around 'C', B (black profile in Fig. 2d and Fig. 3Aa) and the magnetic pressure (P_B; blue in Fig. 3Ae) display a (weak) local depression. MMS2 (Fig. 3Ba and e) also observed a suppressed peak in these profiles around 'C'. This is a so-called 'M'-shaped crater FTE[23]. The plasma pressure (P_{pl}; red profiles in Fig. 3e) was locally enhanced at the center of the FTE. These P_B and P_{pl} variations constitute a relatively single P_{tot} (black profiles in Fig. 3e) enhancement around 'C'.

The B reduction/suppression at 'C' might result from local reconnection. This is supported by the existence of an abrupt change in B_N (rather than sinusoidal bipolar B_N), indicating a local current sheet (red profile in Fig. 2d and Fig. 3a). [Note that the present L, M, and N axes correspond to N, -M, and L axes, respectively, in nominal 2-D reconnection geometry, where L directs along the current sheet and N points to the current sheet normal.] Correspondingly, ion outflow jets directed along N (red arrows in Fig. 3c) and out-of-plane electron jets along M (vertical green arrow in Fig. 3d) carried a significant electric current (Fig. 3m). $\mathbf{J} \cdot \mathbf{E}'$ fluctuated, showing negative values before/around 'C' (Fig. 3n). These observations are consistent with typical signatures of reconnection, particularly under a large guide field[24,25]. The negative (positive) $\mathbf{J} \cdot \mathbf{E}'$ represents a transfer of energy from plasmas to the magnetic fields (from the fields to plasmas). The highly fluctuating $\mathbf{J} \cdot \mathbf{E}'$ indicates strong interactions between the magnetic fields and plasmas with the negative values implying the outer edge of the electron diffusion region[26] or associations with waves[27].

Fig. 5 shows 2-D cuts of 3-D electron distributions at three selected times before, around, and after 'C' (Fig. 5a, b, and c), denoted by black arrows at the bottom of Fig. 3A. The upper and lower panels show the electron distributions as a function of ($V_{\parallel}$, $V_{\perp 1}$) and ($V_{\perp 1}$, $V_{\perp 2}$), respectively. Parallel and perpendicular directions are defined with respect to the local magnetic field ($\mathbf{B}$). The two perpendicular directions are chosen to be perpendicular to $\mathbf{B}$ approximately along the ion bulk velocity ($\mathbf{V}_i$), $\mathbf{V}_{\perp 1} = \mathbf{B}\times(\mathbf{V}_i\times\mathbf{B})$ and $\mathbf{V}_{\perp 2} = \mathbf{B}\times\mathbf{V}_i$.

Fig. 5(a) shows a low-density, high-temperature (Fig. 3b) magnetospheric electron distribution. Fig. 5(c) shows a heated, antiparallel-streaming magnetosheath electron distribution. Fig. 5(b) shows a mixture of the two populations. Note the superposition of a magnetosheath electron population shaped as a half shell in ($-V_{\parallel}$, $V_{\perp 1}$) plane. At the same time, the ($V_{\perp 1}$, $V_{\perp 2}$) distribution shows a certain level of agyrotropy, i.e., a lack of axisymmetry (red arrow in the lower middle panel in comparison to lower left and right panels showing almost gyrotropic distributions). The half-shell shape in the ($V_{\parallel}$, $V_{\perp}$) distributions together with a weak electron agyrotropy indicates the outer edge of the electron diffusion region[26]. These simultaneous observations of B_N reversal, ion outflow jets, out-of-plane electron jets, non-zero $\mathbf{J} \cdot \mathbf{E}'$, and anti-parallel half-shell/slightly agyrotropic electron distribution manifest that reconnection was occurring in the interface between two interlinked flux tubes.

Discussion

Magnetic topology of two interlinked flux tubes. Our analyses indicate that the present FTE consisted of two interlaced flux tubes. The electron PAD showed energy-dependent variations that infer different magnetic topologies[8,28,29] across the center of the FTE (Fig. 3j-l).

In particular, dramatic changes in the electron PADs were observed before and after 'C'. This includes a significant reduction in the low and mid energy electron fluxes (Fig. 3j, k) immediately before ~'C', during ~08:15:02.75-3.20 UT ('A'-~'L' at the top of Fig. 3A) for MMS4 and during ~08:15:02.70-3.15 UT ('A'-~'L' at the top of Fig. 3B) for MMS2. These low (and mid) energy electrons were mostly counter-streaming between ‘L’ and ‘C’, while low-energy electrons were mostly one-directional (anti-parallel) immediately after ~‘C’ during ~08:15:03.20-3.65 UT (~‘L’-‘B’ at the top of Fig. 3A) for MMS4 and during ~08:15:03.15-3.55 UT (~‘L’-‘B’ at the top of Fig. 3B) for MMS2. The 90° pitch-angle electrons were greatly enhanced in the high-energy range (Fig. 3l) only before ‘C’.

These 90°-focused energetic electrons can be either locally energized or trapped on the field lines connected to both hemispheres. The former corresponds to trapped electrons locally bouncing within the exhaust region with a large magnetic gradient/curvature, showing a pitch-angle broadening at magnetic-strength minima in accordance with the first adiabatic invariant[8]. We over-plot black and magenta dotted contours over the electron PADs (Fig. 3j-l) that represent loss-cone angles under an assumption that there is a mirror point with a magnetic strength of 109 nT (black) or 100 nT (magenta). These contours appear to generally separate the 90°-focused energetic population from field-aligned (< ~45°) and weaker anti-parallel (> ~135°) populations (Fig. 3l). This signature is, however, mostly seen before ‘C’, during which the pitch-angle broadening often shows a deviation from the expectation. Furthermore, the locally bouncing/focusing population will result in a balance in fluxes between parallel and anti-parallel components. The parallel population prevails over the anti-parallel throughout the period shown in Fig. 3 (compare Fig. 3g and 3i). There is also an interval during which the anti-parallel population is more dominant (e.g., red arrows at the top of Fig. 3l). Although the former can be explained by the fact that the overall structure was embedded in the southern outflow region of an X-line (Fig. 4b), the latter is hardly explained. Thus, the local energization cannot fully explain these 90°-focused energetic electrons that were exclusively observed before ‘C’, and accompanied by the imbalanced parallel and anti-parallel fluxes.

For electrons being trapped on the field lines with their ends connected to the northern and southern hemispheres, it takes ~5 s (2 s) for 1 keV (10 keV) electrons to travel 5 R_E along the magnetopause field lines. The most energetic electrons on recently-closed field lines (via reconnection at the interface of the two flux tubes) will constitute the 90°-focused population, while less energetic electrons will lead to the imbalance between the parallel and anti-parallel fluxes. On the other hand, the most energetic electrons on early-closed field lines can escape away from the field lines, while less energetic ones remain trapped at 90°. This feature is exactly seen as an inverse energy-time dispersion of high-energy electrons with perpendicular (or anti-parallel) pitch angles (red arrows in Fig. 3h and 3i).

The absence or reduction of these 90°-focused energetic electrons after ‘C’ indicates magnetosheath field lines or open field lines with one end connected to the northern or southern hemisphere (Fig. 3l). During ‘C’-‘T’, the parallel high-energy population was still denser than the anti-parallel one, possibly due to the background effect associated with the location of the overall structure. Before/around ‘B’, a notable reduction in these energetic electrons, together with uni/bi-directional low-energy electrons (Fig. 3j) indicates the magnetosheath field lines (with neither end connected to the hemisphere), on which the low-energy magnetosheath electrons flow along one direction or both directions with respect to **B**.

Thus, the energy-dependent PAD variations across the center of the FTE infer that the two flux tubes contain field lines of different magnetic topologies: one with the field lines connected to both hemispheres and the other with open field lines connected to the magnetosheath. This was further evidenced by the plasma density and temperature (Fig. 3b) and particle distribution functions (Fig. 5).

Fig. 1(b-e) illustrates the generation of such interlinked flux tubes and their connectivity to either both hemispheres or the magnetosheath. For the southward and duskward IMF during this event (Fig. 1b), reconnected field lines at ‘1’ in Fig. 1(c) (generating cyan field lines) can constitute a flux tube ‘ft1’-‘ft2’ in Fig. 1(d), with one end connected to the northern hemisphere. Reconnected field lines at ‘2’ in Fig. 1(c) (generating magenta field lines) can constitute a flux tube ‘ft3’-‘ft4’, with one end connected to the southern hemisphere (Fig. 1d). When the interface of the interlaced flux tubes undergoes reconnection (dashed violet arrows in Fig. 1d), ‘ft1’ and ‘ft4’ field lines are reconnected, constituting “ft C-T” with both ends connected to the magnetosheath (blue arrows in Fig. 1e), and ‘ft2’ and ‘ft3’ field lines are reconnected, constituting “ft L-C” with both ends connected to the magnetosphere (red arrows in Fig. 1e). When these newly intertwined flux tubes move southward/duskward past by MMS4 as depicted by blue arrows in Fig. 1(e) mostly along *L*, “ft L-C” is first traversed by MMS, then, “ft C-T” is traversed, consistent with the observations of Fig. 4(b) and the electron PADs.

We note that the reconnecting flux tubes (Fig. 1d) result in a more complicated structure (Fig. 1e). This structure will exert strong magnetic tension force toward the interface of the two interlinked flux tubes, which facilitates an interaction of the interface. The plasma and field data showed that the two flux tubes were reconnecting at the interface (dashed violet arrows in Fig. 1e). The magnetic curvature, $(\mathbf{B} \cdot \nabla\mathbf{B})_N/\mu_0$ (black in Fig. 2j) reverses its sign from positive to negative across ‘C’, as expected for “ft L-C” and “ft C-T” in Fig. 6d. The strong, clearly-bipolar feature across the FTE center, thus, supports the complicated interlaced flux tubes, Fig. 1e.

The *N* component of the magnetic curvature (black profiles in Fig. 2l) is not balanced by any of the pressure gradients (red, blue, and green profiles in Fig. 2l). The *L* and *M* components (black profiles in Fig. 2i and j) are, however, partly balanced by the gradient of the total pressure, $\boldsymbol{\nabla} P_{\text{tot}}$ (green) or the magnetic pressure ($\boldsymbol{\nabla} P_{\text{B}}$, blue). Around ‘C’, the current density parallel to **B** is larger than the perpendicular component, which is, however, significant ($J_{||}$ = ~1800 nA/m^2; $J_\perp$ = ~1000 nA/m^2; Fig. 2f). These suggest that the FTE is neither force-free nor force-balanced. This might indicate that the FTE was under evolution, explaining the highly variable plasma flows (Fig. 3c, d), current (Fig. 2e, f; Fig. 3m), and $\mathbf{J} \cdot \mathbf{E}'$ (Fig. 2g; Fig. 3n) within the FTE. Depending on the evolutionary phase of the interlinked flux tubes, a portion of field lines within the FTE can be either connected to either hemisphere (Fig. 6c) or both hemispheres (Fig. 6d).

Implications and conclusion. The complex magnetic field topology and various magnetic connectivity including field lines with both ends connected to the magnetosphere within the FTE result from the kinetic process, i.e., reconnection locally occurring at the center of the FTE (not occurring outside or at the periphery of the FTE). This makes a striking distinction from the previous multiple X-line FTE model[3] (Fig. 1a) that can also involve either newly-opened magnetosheath field lines or completely closed field lines within an FTE[28,29]. When connected to both hemispheres, the flux tube becomes an efficient channel for solar wind transfer into the magnetosphere. The resulting complicated structure (Fig. 1e) resembles a typical flux rope structure, and consecutive interface reconnection (e.g., dashed violet arrow in Fig. 1e) will lead further evolution to a flux rope (twining flux tubes). The interlinking of flux tubes will also potentially suppress magnetic flux transfer into the magnetotail, via which FTEs act for the main driver of the magnetospheric dynamics such as substorms and storms[30]. The magnetic connectivity will continuously vary during different epochs in the evolution, both regulating the transfer of the solar wind into the magnetosphere and the magnetic flux transfer from the dayside to the magnetotail.

The importance of the local kinetic processes occurring inside FTEs is, therefore, two-fold. First, they lead to the topological structure and evolution of FTEs. Second, they determine macroscale characteristics of FTEs (magnetic connectivity and magnetic content), including their global effects. Using the MMS observation of the FTE event, we emphasized the importance and impact of one of the local kinetic processes, i.e., reconnection, occurring within FTEs, implying that the kinetic process can play a crucial role in the generation, structure, evolution, and impact of FTEs.

Methods

Instrumentation and data availability. The MMS spacecraft[6] flying in low-inclination and highly elliptical orbits provide the measurements at/near Earth's magnetopause, bow show, and magnetotail. The four spacecraft are identically equipped with instruments including plasma instruments (FPI)[31], magnetometers (FGM)[32], and electric field instruments (EDP) consisting of the spin-plane double probe (SDP)[33] and the axial double probe (ADP)[34]. We used the magnetic field data from FGM with a time resolution of 10-ms in burst mode, the DC electric field data with a 0.122-ms time resolution in burst mode, and particle data in burst mode from the FPI/DIS for ions and FPI/DES for electrons with a 150-ms and 30-ms time resolution, respectively, a 11.25° angular resolution, and an energy range of ~10 eV–26 keV. The MMS data are accessible through the public link provided by the MMS science working group teams: http://lasp.colorado.edu/mms/sdc/public/.

The Moon-orbiting ARTEMIS spacecraft[35], designed to investigate the Moon's interaction with the solar wind, also provide high time resolution (3-s) data of solar wind conditions. We use the data from the fluxgate magnetometer (FGM) and electrostatic analyzer (ESA) to obtain interplanetary magnetic field (IMF) orientation and solar wind speed for the present FTE event. The ARTEMIS data are available at http://themis.ssl.berkeley.edu/. The data were lagged by 13 minutes in this event to account for the transit time of the solar wind from ARTEMIS-C, located at [64.2, 3.3, 3.3]R_E in GSM to MMS at [9.0, -1.2, 1.3]R_E in GSM.

Determination of boundary normal coordinates (LMN). We determined boundary normal coordinates (LMN) by we performing 1) minimum variance analysis (MVA)[16] and 2) minimum directional derivative (MDD) analysis[17]. The former method using the four-spacecraft magnetic field data during 0815:01.0-04.5 UT derived L = [0.35, -0.72, 0.60], M = [0.46, -0.43, -0.78], and N = [0.82, 0.55, 0.17] in GSM. To comply with conventions, N points outward from the magnetopause and L points northward along the dayside magnetopause, partly aligning the magnetospheric magnetic field (see the top of the right panel of Fig. 1a). The medium-to-minimum (maximum-to-medium) eigenvalue ratio was ~3.3 (4.5), indicating a relatively reliable calculation[36]. The MDD result is shown in Fig. 2(b-c). The eigenvector of the matrix, $(\nabla\mathbf{B})(\nabla\mathbf{B})^{\mathrm{T}}$ corresponding to the minimum eigenvalue significantly fluctuated (Fig. 2b). At ~0815:03.5 UT, around which the sign of B_X was reversed (Fig. 2a) and the error was minimized (Fig. 2c), the three eigenvectors of $(\nabla\mathbf{B})(\nabla\mathbf{B})^{\mathrm{T}}$ pointed L = [0.39, -0.61, 0.69], M = [0.45, -0.52, -0.72], and N = [0.80, 0.60, 0.07] in GSM, where M corresponds to the (negative/positive) eigenvector for the minimum eigenvalue of $(\nabla\mathbf{B})(\nabla\mathbf{B})^{\mathrm{T}}$ (Fig. 2b), representing the most invariant axis. The difference between MVA-derived and MDD-derived L, M, and N ranged from 5.8° to 8.3°. We used the averaged MVA and MDD result: L = [0.38, -0.66, 0.65], M = [0.46, -0.48, -0.75], and N = [0.81, 0.58, 0.12] in GSM.

Acknowledgments

This study was supported, in part, by NASA's MMS project at SwRI, NSF AGS-1834451, AGS-1907698, NASA 80NSSC18K1534, 80NSSC18K0570, 80NSSC18K0693, 80NSSC18K1337, 80NSSC18K0657, and ISSI program: MMS and Cluster observations of magnetic reconnection. MMS datasets were provided by the MMS science working group teams through the link (http//lasp.colorado.edu/mms/sdc/public/). The ARTEMIS data are available at http://themis.ssl.berkeley.edu. KJH thanks and acknowledges MMS instrument teams for providing data.

References

1. Cooling, B. M. A. Role of the magnetosheath flow in determining the motion of open flux tubes. **106**, (2001).
2. Russell, C. T. & Elphic, R. C. Initial ISEE magnetometer results: magnetopause observations. *Space Sci. Rev.* (1978). doi:10.1007/BF00212619
3. Lee, L. C. & Fu, Z. F. A theory of magnetic flux transfer at the Earth's magnetopause. *Geophys. Res. Lett.* **12**, 105–108 (1985).
4. Scholer, M. Magnetic flux transfer at the magnetopause based on single X line bursty reconnection. *Geophys. Res. Lett.* (1988). doi:10.1029/GL015i004p00291
5. Fear, R. C. *et al. Motion of flux transfer events: a test of the Cooling model*. **25**, (2007).
6. Burch, J. L. *et al*. Magnetospheric Multiscale Overview and Science Objectives. *Sp. Sci Rev* 5–21 (2016). doi:10.1007/s11214-015-0164-9
7. Eastwood, J. P. *et al.* Ion-scale secondary flux ropes generated by magnetopause reconnection as resolved by MMS. 4716–4724 (2016). doi:10.1002/2016GL068747.Received
8. Hwang, K. J. *et al.* Small-Scale Flux Transfer Events Formed in the Reconnection Exhaust Region Between Two X Lines. *J. Geophys. Res. Sp. Phys.* **123**, 8473–8488 (2018).
9. Hwang, K. J. *et al.* The substructure of a flux transfer event observed by the MMS spacecraft. *Geophys. Res. Lett.* **43**, 9434–9443 (2016).
10. Zhou, M. *et al.* Coalescence of Macroscopic Flux Ropes at the Subsolar Magnetopause : Magnetospheric Multiscale Observations. **055101**, 1–6 (2017).
11. Wang, R. *et al.* Interaction of Magnetic Flux Ropes Via Magnetic Reconnection Observed at the Magnetopause. *J. Geophys. Res. Sp. Phys.* **122**, 10,436-10,447 (2017).
12. Øieroset, M. *et al.* MMS observations of large guide field symmetric reconnection between colliding reconnection jets at the center of a magnetic flux rope at the magnetopause. 5536–5544 (2016). doi:10.1002/2016GL069166.Received
13. Øieroset, M. *et al.* Reconnection With Magnetic Flux Pileup at the Interface of Converging Jets at the Magnetopause. *Geophys. Res. Lett.* **46**, 1937–1946 (2019).
14. Kacem, I. *et al.* Magnetic Reconnection at a Thin Current Sheet Separating Two Interlaced Flux Tubes at the Earth's Magnetopause. *J. Geophys. Res. Sp. Phys.* **123**, 1779–1793 (2018).
15. Zhong, Z. H. *et al.* Evidence for Secondary Flux Rope Generated by the Electron Kelvin-Helmholtz Instability in a Magnetic Reconnection Diffusion Region. *Phys. Rev. Lett.* **120**, 75101 (2018).
16. Sonnerup, B. & Scheible, M. Minimum and maximum variance analysis. *Anal. methods Multi-spacecr. data* **001**, 185–220 (1998).
17. Szscoe, G. L. & Angeles, L. Significance Criteria for Variance Matrix Applications = Y]

and cumulative distributions for the case. **77**, 1–2 (1972).

18. Zhou, X. Z. *et al.* Multiple triangulation analysis: Application to determine the velocity of 2-D structures. *Ann. Geophys.* **24**, 3173–3177 (2006).
19. Russell, C. T., Mellott, M. M., Smith, E. J. & King, J. H. Multiple Spacecraft Observations of Interplanetary Shocks: Four Spacecraft Determination of Shock Normals. **88**, 4739–4748 (1983).
20. Paschmann, G. *et al. Reprinted from Analysis Methods for Multi-Spacecraft Data Tetrahedron Geometric Factors 13.1 Introduction*. (1998).
21. Trattner, K. J., Petrinec, S. M., Fuselier, S. A. & Phan, T. D. The location of reconnection at the magnetopause : Testing the maximum magnetic shear model with THEMIS observations. **117**, 1–12 (2012).
22. Louarn, P. *et al.* Cluster observations of complex 3D magnetic structures at the magnetopause. *Geophys. Res. Lett.* **31**, (2004).
23. Labelle, J. *et al. AMPTE IRM Observations of Waves Associated With Flux Transfer Events in the Magnetosphere*. *JOURNAL OF GEOPHYSICAL RESEARCH* **92**, (1987).
24. Eriksson, S. *et al.* Magnetospheric Multiscale Observations of the Electron Diffusion Region of Large Guide Field Magnetic Reconnection. **015001**, 1–6 (2016).
25. Nakamura, T. K. M. *et al.* Turbulent mass transfer caused by vortex induced reconnection in collisionless magnetospheric plasmas. *Nat. Commun.* **8**, 1–8 (2017).
26. Hwang, K. J. *et al.* Magnetospheric Multiscale mission observations of the outer electron diffusion region. *Geophys. Res. Lett.* **44**, 2049–2059 (2017).
27. Swisdak, M. *et al.* Localized and Intense Energy Conversion in the Diffusion Region of Asymmetric Magnetic Reconnection. *Geophys. Res. Lett.* **45**, 5260–5267 (2018).
28. Pu, Z. Y. *et al.* Magnetic topologies of an in vivo FTE observed by Double Star / TC-1 at Earth ' s magnetopause. **40**, 3502–3506 (2013).
29. Zhong, J. *et al.* Three-dimensional magnetic fl ux rope structure formed by multiple sequential X-line reconnection at the magnetopause. **118**, 1904–1911 (2013).
30. Fear, R. C., Trenchi, L., Coxon, J. C. & Milan, S. E. How Much Flux Does a Flux Transfer Event Transfer? *J. Geophys. Res. Sp. Phys.* **122**, 12310–12327 (2017).
31. Pollock, C. *et al.* Fast Plasma Investigation for Magnetospheric Multiscale. *Space Sci. Rev.* **199**, 331–406 (2016).
32. Russell, C. T. *et al.* The Magnetospheric Multiscale Magnetometers. *Space Sci. Rev.* **199**, 189–256 (2016).
33. Lindqvist, P. A. *et al.* The Spin-Plane Double Probe Electric Field Instrument for MMS. *Space Science Reviews* (2016). doi:10.1007/s11214-014-0116-9
34. Ergun, R. E. *et al.* The Axial Double Probe and Fields Signal Processing for the MMS Mission. *Space Sci. Rev.* **199**, 167–188 (2016).
35. Angelopoulos, V. The ARTEMIS mission. *Space Sci. Rev.* **165**, 3–25 (2011).

36. Shi, Q. Q. *et al.* Dimensional analysis of observed structures using multipoint magnetic field measurements : Application to Cluster. **32**, 1–5 (2005).

37. Fear, R. C. *et al. The azimuthal extent of three flux transfer events*. **26**, (2008).

38. Dunlop, M. W., Balogh, A. & Robert, P. Four-point Cluster application of magnetic field analysis tools : The Curlometer. **107**, 1–14 (2002).

38. Lundquist, S., Magnetohydrostatic fields, *Ark. Fys*, **2**, 361–365 (1950).

Figure 1. (a) The multiple X-line FTE model for the southward and dawnward IMF. The unreconnected magnetospheric and magnetosheath magnetic field lines are shown by black and blue arrows, respectively. Red arrows represent reconnected magnetic field lines. The edge of the FTE is shown in green. The left panel shows a view from the Sun (the normal to the magnetopause surface) and the right panel shows a view from dawn to dusk (along the direction tangential to the magnetopause). The nominal LMN coordinates for the FTE are shown at the top of the right panel. (b-d) Illustration of the generation of interlinked flux tubes under the southward and duskward IMF and (e) their connectivity to either hemisphere or both hemispheres: reconnected field lines at '1' in (c) (generating cyan field lines) can constitute a flux tube 'ft1'-'ft2' in (d), with one end connected to the northern hemisphere. Reconnected field lines at '2' in (c) (generating magenta field lines) can constitute a flux tube 'ft3'-'ft4', with one end connected to the southern hemisphere (d). When the interface of the interlaced flux tubes undergoes consecutive reconnection (dashed violet arrows in d), 'ft1' and 'ft4' field lines are reconnected, constituting "ft C-T" with both ends open (blue arrows in e), and 'ft2' and 'ft3' field lines are reconnected, constituting "ft L-C" with both ends connected to the magnetosphere (red arrows in e).

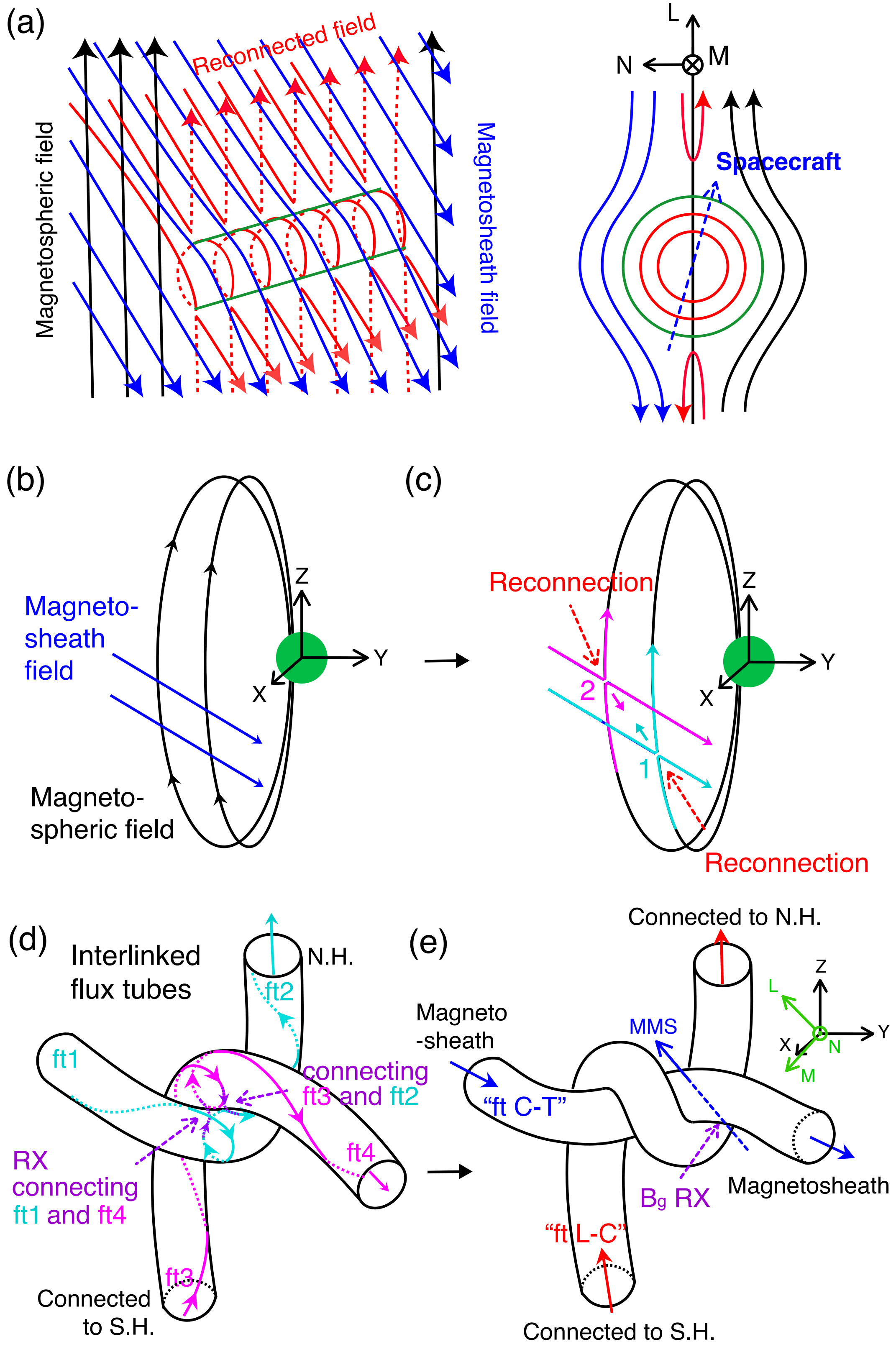

(a)
Reconnected field
Magnetospheric field
Magnetosheath field
L
N
M
Spacecraft
(b)
Magneto-
sheath
field
Magneto-
spheric field
Z
Y
X
(c)
Reconnection
2
1
Reconnection
Z
Y
X
(d)
Interlinked
flux tubes
N.H.
ft2
ft1
connecting
ft3 and ft2
ft4
RX
connecting
ft1 and ft4
ft3
Connected
to S.H.
(e)
Connected to N.H.
Magneto
-sheath
"ft C-T"
MMS
Z
L
Y
X
N
M
Bg RX
Magnetosheath
"ft L-C"
Connected to S.H.

Figure 2. Four MMS observations of an FTE detected on 18 December, 2017: (a) the tetrahedral-averaged magnetic field using the measurements from the four MMS spacecraft: B_X, B_Y, and B_Z components (blue, green, and red profiles) in GSM, together with the magnetic strength (B; black); (b) the result of minimum directional derivative (MDD) analysis[17] showing the eigenvector of the matrix, $(\nabla\mathbf{B})(\nabla\mathbf{B})^{\mathrm{T}}$ in GSM, corresponding to the minimum eigenvalue, with an error indicator, $|\nabla\cdot\mathbf{B}|/|\nabla\times\mathbf{B}|$ (c). All vector parameters in the lower panels are shown in boundary normal coordinates, LMN that were determined from minimum variance analysis (MVA)[16] and MDD[17]: L = [0.39, -0.61, 0.69], M = [0.45, -0.52, -0.72], N = [0.80, 0.60, 0.07] in GSM: (d) the tetrahedral-averaged magnetic field (**B**) with B_L, B_M, and B_N components (blue, green, and red profiles), together with the magnetic strength (black); (e, f) the current densities (**J**; e) that are decomposed into two components (f) parallel (blue profiles; $J_{||}$) and perpendicular (red; $J_\perp$) to **B** calculated from the curlometer technique[38]; (g) Joule dissipation in the electron rest frame, $\mathbf{J}\cdot\mathbf{E}'$, where $\mathbf{E}'$ is the electric field in the electron frame of reference, $\mathbf{E}'=\mathbf{E}+\mathbf{V}_e\times\mathbf{B}$; (h-j) the L, M, N component of the magnetic curvature, $(\mathbf{B}\cdot\nabla\mathbf{B})/\mu_0$ (black) and the gradients of the total pressure ($\boldsymbol{\nabla}P_{\mathrm{tot}}$, green), the plasma pressure ($\boldsymbol{\nabla}P_{\mathrm{pl}}$, red), and the magnetic pressure ($\boldsymbol{\nabla}P_{\mathrm{B}}$, blue); (k) ion flow vorticity ($\boldsymbol{\Omega}_{\mathrm{i}} = \nabla\times\mathbf{V}_i$). Vertical dashed magenta, black, and cyan lines denote the leading edge, center, and trailing edge of the FTE.

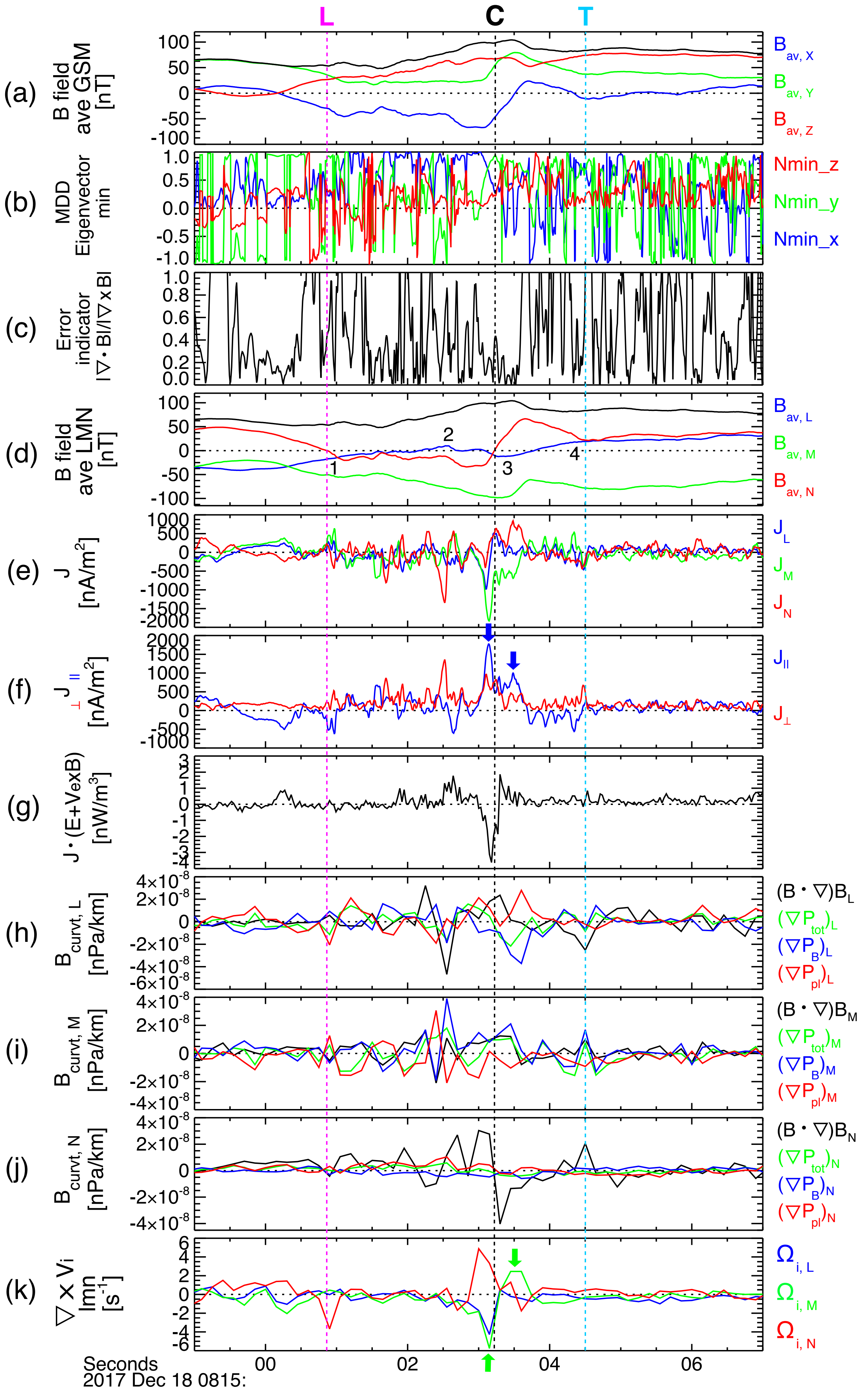

L
C
T
(a)
B field ave GSM [nT]
$B_{av, X}$
$B_{av, Y}$
$B_{av, Z}$
(b)
MDD Eigenvector min
Nmin_z
Nmin_y
Nmin_x
(c)
Error indicator |∇·B|/|∇xB|
(d)
B field ave LMN [nT]
$B_{av, L}$
$B_{av, M}$
$B_{av, N}$
1
2
3
4
(e)
J [nA/m^2]
J_L
J_M
J_N
(f)
$J_{\perp}$ $J_{\parallel}$ [nA/m^2]
$J_{\parallel}$
$J_{\perp}$
(g)
J·(E+VexB) [nW/m^3]
(h)
$B_{curvt, L}$ [nPa/km]
$(B\cdot\nabla)B_L$
$(\nabla P_{tot})_L$
$(\nabla P_B)_L$
$(\nabla P_{pl})_L$
(i)
$B_{curvt, M}$ [nPa/km]
$(B\cdot\nabla)B_M$
$(\nabla P_{tot})_M$
$(\nabla P_B)_M$
$(\nabla P_{pl})_M$
(j)
$B_{curvt, N}$ [nPa/km]
$(B\cdot\nabla)B_N$
$(\nabla P_{tot})_N$
$(\nabla P_B)_N$
$(\nabla P_{pl})_N$
(k)
∇ × Vi lmn [s^{-1}]
$\Omega_{i, L}$
$\Omega_{i, M}$
$\Omega_{i, N}$
Seconds
2017 Dec 18 0815:
00
02
04
06

Figure 3. MMS4 (A) and MMS2 (B) observations of the FTE: (a) magnetic field (**B**), B_L, B_M, and B_N components (blue, green, and red profiles), together with the magnetic strength (black); (b) ion density (black) and temperature (red); (c) ion velocity ($\mathbf{V_i}$); (d) electron velocity ($\mathbf{V_e}$); (e) plasma (red) and magnetic (blue) pressures, and the sum of plasma and magnetic pressures (black); (f) ion pitch angle distribution (PAD); (g-i) energy spectrograms of electrons of parallel (0°~30°; g), perpendicular (60°~120°; h), and anti-parallel (150°~180°; i) pitch angles; (j-l) pitch angle distributions (PAD) of the low- (~10 eV ≤ energy < 100 eV; j), mid- (100 eV ≤ energy < 1 keV; k), and high- (1 keV ≤ energy < 26 keV; l) energy electrons; (m) the current densities obtained from the particle data; (n) Joule dissipation in the electron rest frame, $\mathbf{J}\cdot\mathbf{E}'$, using the single spacecraft data. All vector parameters are shown in LMN coordinates. Vertical dashed dashed magenta, black, and cyan lines denote the leading edge, center, and trailing edge of the FTE. Vertical dashed red and black lines mark the location where abrupt changes in the low and mid energy electron fluxes (Fig. 3j, k) appear.

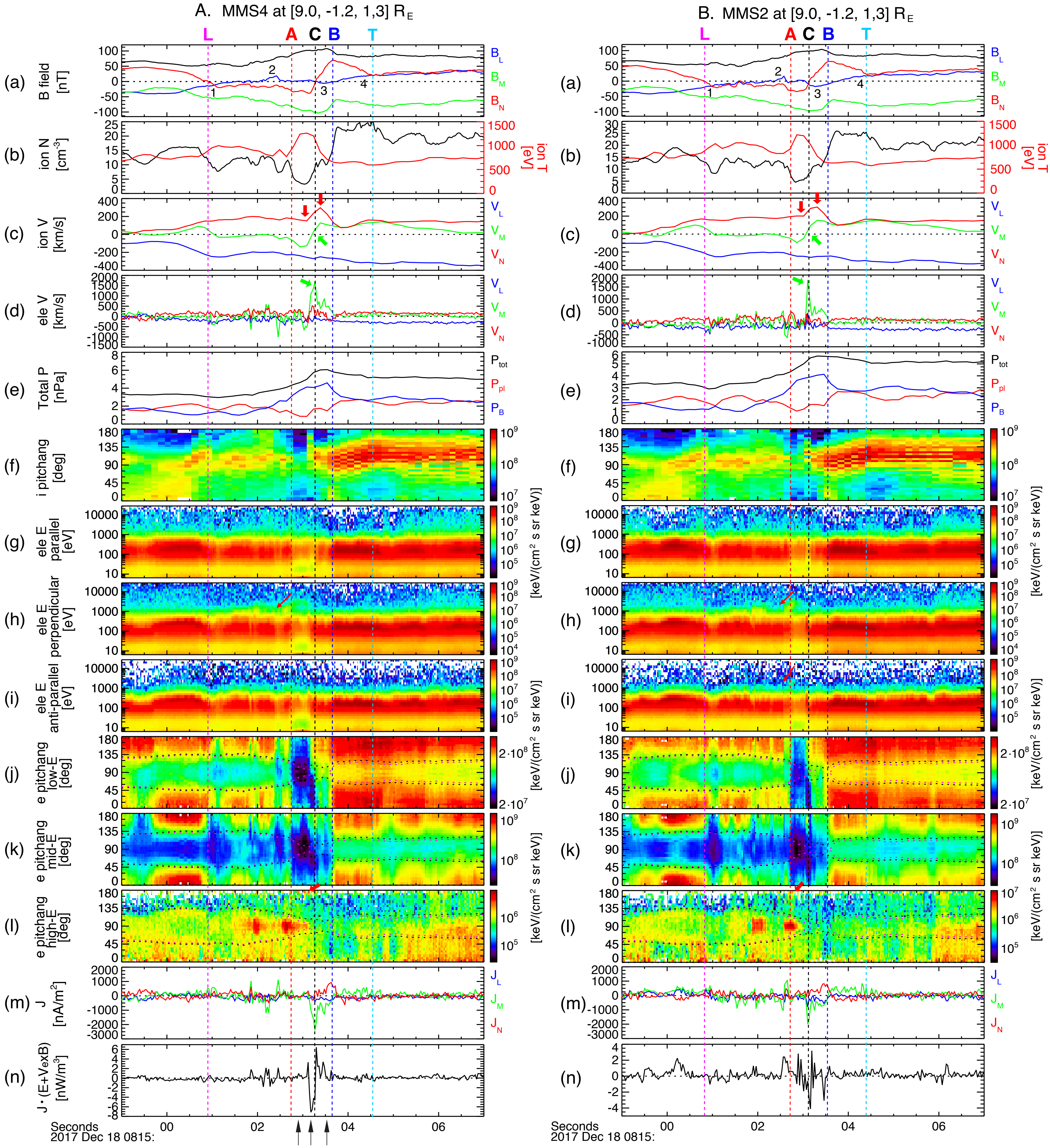
A. MMS4 at [9.0, -1.2, 1,3] R_E
B. MMS2 at [9.0, -1.2, 1,3] R_E
L A C B T
(a) B field [nT]
(b) ion N [cm^-3]
ion T [eV]
(c) ion V [km/s]
(d) ele V [km/s]
(e) Total P [nPa]
P_tot P_pl P_B
(f) i pitchang [deg]
(g) ele E parallel [eV]
(h) ele E perpendicular [eV]
(i) ele E anti-parallel [eV]
(j) e pitchang low-E [deg]
(k) e pitchang mid-E [deg]
(l) e pitchang high-E [deg]
[keV/(cm^2 s sr keV)]
(m) J [nA/m^2]
(n) J • (E+VexB) [nW/m^3]
Seconds
2017 Dec 18 0815:
00 02 04 06

Figure 4. Modeled shear angles between the magnetosheath and magnetospheric magnetic field lines using the solar wind IMF condition and Earth's dipole tilt for the event shown in Fig. 2 and 3 (a). White traces represent primary X-lines over the surface of the magnetopause when viewed from the Sun. A blue rectangle denotes the location of the MMS spacecraft. Black lines and a thick magenta arrow show the model prediction and the observation, respectively, of the plasma bulk flow or the motion of the FTE observed at the MMS location. (b) a schematic diagram of the FTE structure consisting of two interlinked flux tubes embedded in the southern outflow region of the reconnection X-line when viewed mostly from the -*M* direction.

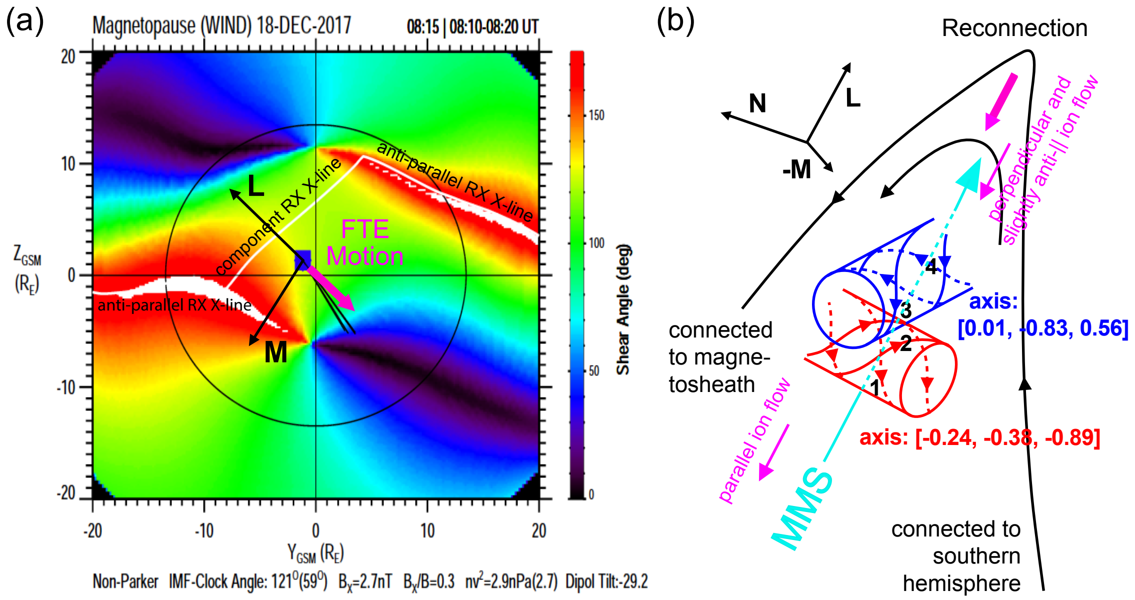

(a)
Magnetopause (WIND) 18-DEC-2017
08:15 | 08:10-08:20 UT
anti-parallel RX X-line
component RX X-line
anti-parallel RX X-line
L
M
FTE
Motion
Z_GSM (R_E)
Y_GSM (R_E)
Shear Angle (deg)
Non-Parker IMF-Clock Angle: 121°(59°) B_X=2.7nT B_X/B=0.3 nv²=2.9nPa(2.7) Dipol Tilt:-29.2
(b)
Reconnection
N
L
-M
perpendicular and slightly anti-|| ion flow
connected to magne-tosheath
axis: [0.01, -0.83, 0.56]
axis: [-0.24, -0.38, -0.89]
parallel ion flow
MMS
connected to southern hemisphere
1
2
3
4

Figure 5. MMS4 observations of 2-D cuts of 3-D electron distributions (integrated over ±11.25° from the cut) at three selected times before, around, and after the center of FTE (a, b, and c), denoted by black arrows at the bottom of Fig. 3A. The upper and lower panels show the electron distributions as a function of ($V_{\|}$, $V_{\perp 1}$) and ($V_{\perp 1}$, $V_{\perp 2}$), respectively. Parallel and perpendicular directions are defined with respect to the local magnetic field (**B**). The two perpendicular directions are chosen to be perpendicular to **B** approximately along the ion bulk velocity velocity ($\mathbf{V}_i$), $\mathbf{V}_{\perp 1} = \mathbf{B}\times(\mathbf{V}_i\times\mathbf{B})$ and $\mathbf{V}_{\perp 2} = \mathbf{B}\times\mathbf{V}_i$. A lack of axisymmetry in the ($V_{\perp 1}$, $V_{\perp 2}$) distribution is denoted by a red arrow in the lower middle panel in comparison to lower left and right panels showing almost gyrotropic distributions.

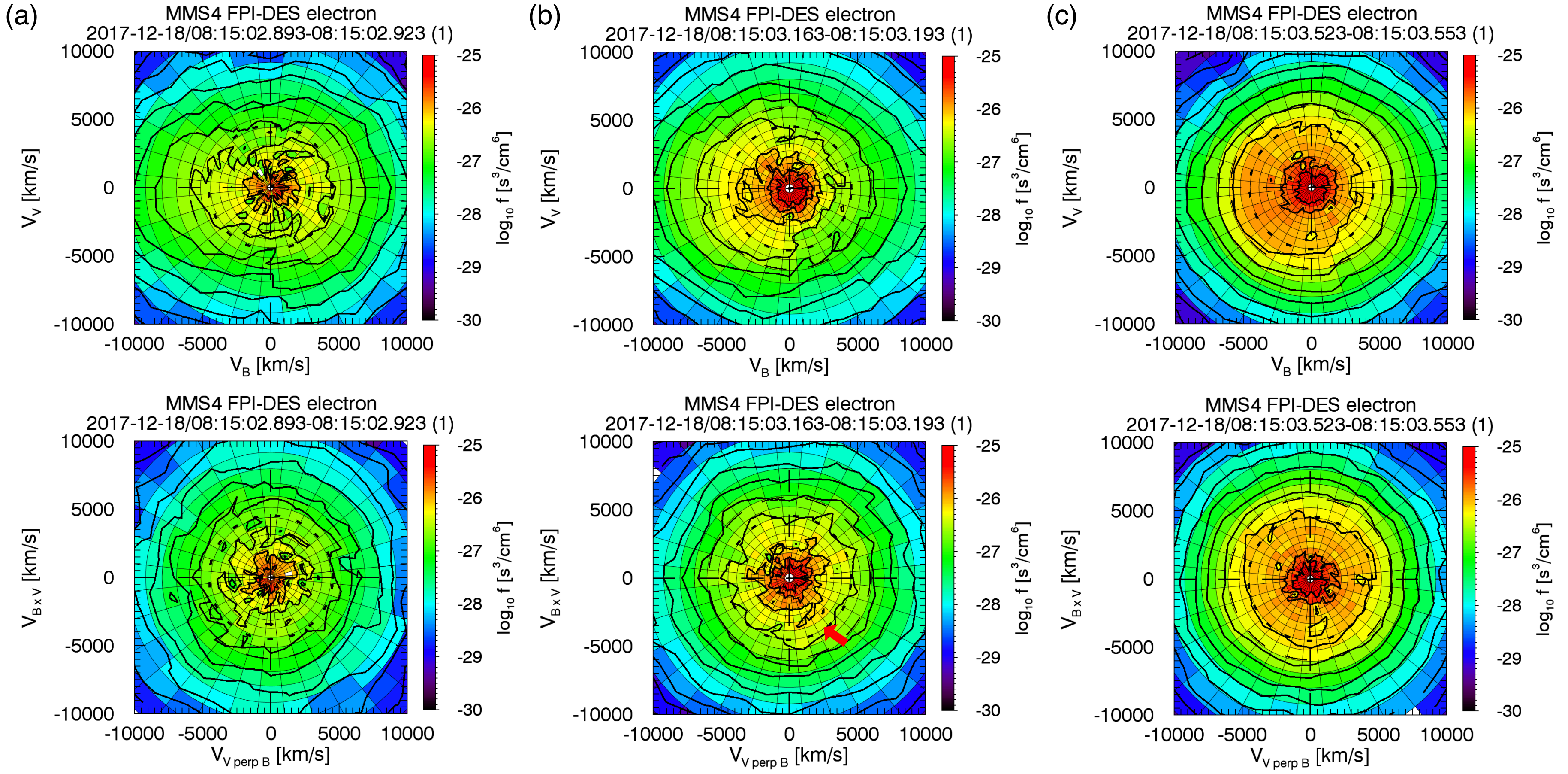
(a)
(b)
(c)
MMS4 FPI-DES electron
2017-12-18/08:15:02.893-08:15:02.923 (1)
2017-12-18/08:15:03.163-08:15:03.193 (1)
2017-12-18/08:15:03.523-08:15:03.553 (1)
V_V [km/s]
V_B [km/s]
V_BxV [km/s]
V_V perp B [km/s]
log10 f [s^3/cm^6]
10000
5000
0
-5000
-10000
-25
-26
-27
-28
-29
-30